PSFC/JA-00-3

Omegatron Ion Mass Spectrometer for the Alcator C-Mod Tokamak

R. Nachtrieb[a], B. LaBombard, E. Thomas, Jr.[b]

MIT Plasma Science and Fusion Center, Cambridge MA, 02139-4213, USA

[a] *Lutron Electronics Co., Inc., Coopersburg, PA 18036 USA*

[b] *Physics Department, Auburn University, AL, 36849-5311, USA*

(March 18, 2000)

Abstract

A new ion mass spectrometry probe that operates at high magnetic field (~ 8 tesla) has been recently commissioned on the Alcator C-Mod tokamak. The probe combines an omegatron $\mathbf{E}(t)\times\mathbf{B}$ ion mass spectrometer and a retarding field energy analyzer. The probe samples the plasma in the far scrape-off layer (SOL), on flux surfaces between 25 and 50 millimeters from the separatrix. Radio frequency (RF) power is used to collect ions with resonant cyclotron frequency on the side walls of an RF cavity. Scanning the frequency results in a spectrum ordered by the ratio of ion mass to charge, M/Z. Resonances are presently resolved for $1 \leq M/Z < 12$ down to signal levels as low as 5×10^{-4} times that of the bulk plasma species. Well-resolved resonances have widths within a factor of two of theoretical values obtained from particle orbit theory. Absolute impurity fluxes and individual impurity charge state temperatures are quantified by varying the applied RF power and recording the change of the amplitude of the resonant ion current. The design of the hardware and electronics design is described, the principles of operation are discussed, and

initial experimental results are presented. Sources of noise which presently limit the sensitivity of the device are also discussed along with techniques to improve the signal to noise ratio.

I. INTRODUCTION

The edge plasma of a magnetic fusion reactor plays an important role in the reactor's performance because of its influence on: plasma heat distribution to the vessel wall; core particle and energy confinement properties; introduction of fusion fuel into the core; sources of impurities which penetrate into the core plasma; and removal of helium ash from edge.[1] A complete model of the edge plasma is difficult to realize due to the many active processes in the edge, and validation of any type of model relies heavily on experimental data. Ion mass spectrometry complements the typical suite of edge plasma diagnostics, which includes Langmuir probes, visible spectroscopy, bolometry, Thomson laser scattering, residual gas analysis, and neutral pressure gauges. The objectives of ion mass spectrometry are to obtain a spectrum of the ion species in the edge plasma, to measure the absolute concentrations of the species, and if possible to determine the temperatures of individual ion species.

Matthews was the first to employ in-situ ion mass spectrometry on a tokamak (DITE), and in his original paper[2] he enumerated the particular requirements of a spectrometer probe: (1) The instrument had to exploit or be immune to the strong magnetic field, (2) the instrument had to accomodate a spread in ion velocities, (3) the geometry had to allow for ion motion parallel to the magnetic field, and (4) the geometry had to be simple to permit calculation of ion transmission. Matthews also mentioned many of the particular challenges: (5) The probe had to be aligned to within a few degrees with the local magnetic field, (6) the intensity of the ion source in the boundary plasma necessitated an attenuating slit to avoid space charge effects, and (7) the noisy electromagnetic environment of the tokamak set the noise and limited the bandwidth of the electronics. Matthews conclusively demonstrated the utility of ion mass spectrometry for helping to diagnose the edge plasma conditions in tokamaks, and the UK Atomic Energy Agency developed his plasma ion mass spectrometer (PIMS) probe into a commercial product.

The ion selectivity of the PIMS probe is based on the mass dependence of the radius of the cycloidal $\mathbf{E} \times \mathbf{B}$ drift orbit that passes through a series of close-spaced apertures. One

drawback of this approach is the necessity to use increasingly smaller aperture structures as the ambient magnetic field is increased. At present the PIMS probe has a maximum magnetic field limit of $\sim$ 3 tesla and cannot be used on Alcator C-Mod,[3] which has a typical toroidal field 4–8 tesla. In principle an omegatron IMS does not have a restriction on magnetic field strength and therefore was considered for Alcator C-Mod.

In 1949 Hipple *et al*[4] determined the proton to electron mass ratio with a device they called an *omegatron*. They employed a permanent magnet, confined protons axially with a dc electric field parallel to magnetic field, and applied a variable frequency radio frequency (RF) electric field at right angle to the magnetic field. The proton cyclotron frequency ω was determined by finding the resonant frequency that caused the proton larmor radii to increase until they were collected on side plates and measured with an amplifier. Subsequently the omegatron concept was used to analyze the composition of low pressure gas systems,[5,6] and at one time a commercial residual gas analyzer based on the omegatron was available.[7] Widespread commercial use of the omegatron ceased with the introduction of the radio frequency quadrupole residual gas analyzer.

More recently, omegatron ion mass spectrometers have been sucessfully operated in linear plasma devices with low magnetic field strength, $B \approx 0.13\,\mathrm{T}$.[8,9] Following initial construction and testing of a prototype unit on a linear plasma device[10] we have successfully constructed and operated an omegatron ion mass spectrometer in the scrape-off layer of a high-field ($4 \leq B\,[\mathrm{T}] \leq 8$) high power density plasma fusion research reactor, Alcator C-Mod.

Section II describes the omegatron concept as implemented on Alcator C-Mod. Section III describes the design of the omegatron probe vacuum hardware, and mentions construction techniques required for robust operation. Section IV describes the design of the low current ammeter electronics with high common mode rejection. Techniques to maximize signal-to-noise ratios are mentioned. Section V describes the theory of plasma interaction with the omegatron and provides formulae used to interpret experimental results. Section VI presents the initial experimental results obtained with the omegatron probe, compares the results with simple theoretical predictions, and discusses sources of noise and further techniques

that may be employed to reduce it.

II. OMEGATRON ON ALCATOR C-MOD

Figures 1–2 show the omegatron probe on Alcator C-Mod, inserted into the upper divertor region of a typical plasma equilibrium. Figure 3 shows a schematic of the key features of the omegatron probe. The probe combines a retarding field energy analyzer (RFEA) with an omegatron ion mass spectrometer. The RFEA is used to diagnose the electron and bulk ion distribution functions as well as to control the parallel energy of ions entering the ion mass spectrometer. The RFEA can also be used to send an energetic beam of electrons down the axis of the omegatron to allow it to operate as a residual gas analyzer.

RF power is used to collect ions with resonant cyclotron frequency on the side walls of an RF cavity. Scanning the frequency results in a spectrum ordered by the ratio of ion mass to charge, M/Z. Independent control of the electric field amplitude permits trading improved mass resolution for collection efficiency. Since the Larmor radius of resonant ions is made to increase, the high magnetic field of Alcator C-Mod does not fundamentally restrict the size of the RF cavity.

In addition to the measurement objectives, the design of the omegatron on Alcator C-Mod satisfies severe engineering constraints: all vaccum components fit inside a vertical diagnostic port 75 mm in diameter and two meters from the plasma, and vacuum components withstand the considerable heat loads that result from plasma disruptions.

The probe internal components are protected from plasma heat flux by a molybdenum heat shield, which is connected electrically to the vacuum vessel. Inside the heat shield is an electrically isolated shield box which contains the retarding field energy analyzer and ion mass spectrometer. The axis of the probe is aligned along the local magnetic field, which is predominantly in the toroidal direction. Plasma flows along field lines through holes in the heat shield and shield box and is attenuated by a tungsten slit before encountering the three grids that constitute the retarding field energy analyzer. Ions and electrons that

traverse the grids enter the RF cavity. Ions in the cavity that have cyclotron frequency $1 \leq f_c\,[\mathrm{MHz}] \leq 100$ close to the frequency of applied RF power are called resonant ions; they absorb RF power and increase their perpendicular energy until they collide with the RF plates. Electrons and non-resonant ions pass through the RF cavity and are collected at the end plate. An isolation transformer provides a DC break and divides the RF power between the two RF plates, each 180 degrees out of phase with the other; a $100\,\Omega$ load between the RF plates provides impedance matching for a wide range of RF frequencies and results in a virtual null in the RF electric field along the axis between the RF plates. Resonant ion current collected on the RF plates is removed through a center-tap of the transformer. The slit, each of the grids, the RF plates, and the end plate each have independent bias control. Current to each component is measured separately, which permits full particle accounting inside the omegatron.

In addition to the retarding field energy analyzer and ion mass spectrometer, the omegatron probe includes three independent Langmuir probes on the face of the heat shield at different radii, which can be used to obtain local cross-field flux profiles of the background plasma. The bulk temperature of the heat shield is measured by two thermocouple junctions. Vertical position of the omegatron is controlled by a linear-motion vacuum bellows and a stepping motor. The bellows are customized to permit $\pm$ 6 degrees of rotational adjustment to align the probe with the magnetic field.

III. OMEGATRON PROBE HEAD

A. Internal Components

Figure 4 shows an exploded view of the retarding field energy analyzer and ion mass spectrometer components. The slit assembly consists of knife-edged pieces of tungsten coated with nickel and spot-welded together. The knife-edge geometry is similar to that of Wan,[11] with one side flat and the other cut at forty-five degrees. The two flat sides face the plasma.

The gap between the knife edges presents an area 25 μm by 7 mm through which the plasma may flow.

Behind the slit assembly are three grids, made from 150 lines-per-inch (nominal) rectangular tungsten mesh, spot-welded to laser cut stainless steel window frames. The grids have line thickness $d = 24.5$ μm and space between grid lines $s = 144$ μm. Optical transmission is estimated by $s^2/(s+d)^2 = 73\%$, which agrees quite well with the the 71% optical transmission obtained by counting pixels in a magnified CCD image of the grid. Each grid window frame has a tab for a wire, by which a voltage bias may be applied and from which current may be collected.

The grids are isolated electrically from each other by laser-cut mica window frame spacers, with approximately 0.7 mm spacing between grids (including the mica spacers and stainless frames). The slit and grids are packed together and are isolated electrically from the side walls of the shield box using ceramic collar pieces. The grids are isolated from the floor of the shield box by a laser-cut mica sheet. The slit and shield box are electrically connected together: a shimstock windowframe spring washer between the slit assembly and the shield box maintains electrical contact and mechanically compresses together the slit assembly, mica spacers, and grids.

The probe head is designed to fit inside the circular portion of an Alcator vertical diagnostic port, which has an inner diameter of 75 mm. This sets an upper bound on the length and width of the RF plates of omegatron ion mass spectrometer. The choice of plate spacing is a compromise between improving resonance resolution (improves as spacing increases) and reducing required RF power (decreases as spacing decreases). The RF plates are made from 0.5 mm thick stainless steel shim stock. Each RF plate is approximately 30 mm wide and 40 mm long. The RF plates are supported mechanically by cylindrical ceramic spacers underneath, between, and on top of the plates. The orientation of the spacers is preserved by short ceramic dowels which pass through the spacers and plates and into recessed holes in the floor of the shield box and in the shield box coverplate. The coverplate and shield box effectively sandwich the RF plates together and provide a uniform spacing of 5 mm between

the RF plates.

Wires soldered to the RF plates deliver the RF power and remove the collected resonant ion current. Four RF resistors (400 Ω, 10 W each) are connected in parallel to the RF plates to give a 100 Ω load for the two 50 Ω coaxial lines connected in series. Short loops of stainless steel wire provide electrical connection with low mechanical stress between the RF resistors and the RF plates. The wires are connected to the plates with high temperature (200° C) silver solder. Each resistor has an electrically isolated tinned copper base which acts as a heat-sink. Through-holes in the resistor bases are tapped so that each resistor can be screwed to the side wall of the shield box. Silver foil between the copper base and shield box ensures that RF power dissipated in the resistor can be transferred to the shield box. The power rating of the RF resistors approaches zero at 150° C, which sets the upper limit of the operating temperature. The upper limit of the non-operation temperature is approximately 200° C (bake-out), set by the teflon insulation in SMA connectors and silver solder connections.

The end collector is electrically isolated from the shield box and is used to remove electrons and non-resonant ions from the cavity. A tab provides space for a wire by which bias may be applied to the end collector and collected current removed. Two ceramic collars fit around the side edges of the end collector to secure it from moving in the plane of the cavity floor. Mica sheets which line the floor of the cavity and the underside of the cavity cover complete the electrical isolation. A band of annealed shim stock is spot-welded to the end collector and wrapped around the middle of the two rear RF plate ceramic support posts. The band collects non-resonant current that might otherwise strike the posts and charge them to a floating potential.

B. External Components

Figure 5 shows the external components of the omegatron probe head, including the heat shield, the shield box and shield box coverplate, the patch panel, the lock plate, the mounting

plate and the angled adapter piece. The internal components of the omegatron probe are protected from the scrape-off layer plasma heat flux by a molybdenum heat shield. The face of the heat shield has an elongated opening that lines up with the slit, and recessions for Langmuir probes below the slit (LP1, closer to the plasma), in line with the slit (LP2), and above the slit (LP3, further from the plasma). The heat shield also has two vertical holes for thermocouples. The heat shield has a recession into which a copper cooling finger is inserted. The cooling finger is attached to the end of a re-entrant tube. Compressed air is blown on the end of the cooling finger through a stainless steel tube inserted into the re-entrant tube. When the omegatron head is inserted into a tokamak discharge the bulk temperature of the heat shield can increase from 30° C to 50° C, and up to 90° C after an upward-going disruption. With the compressed-air cooling on, the temperature of the heat shield drops by 20° C in the ten minutes between discharges; with the compressed-air cooling off the temperature of the heat shield drops only a few degrees in ten minutes.

The shield box fits into a recession in the heat shield and contains the assembled components of the retarding field energy analyzer and ion mass spectrometer. The shield box is made from stainless steel with a flame-sprayed aluminum-oxide coating on the outside to isolate the shield box from the heat shield. The shield box has an elongated opening that lines up with the slit (inside) and the heat shield elongated opening (outside). The floor of the shield box has four recessions for the ends of the ceramic dowels that maintain the alignment of the RF plates and ceramic spacers. Inside the shield box near the front and back are lips which hold the grid assembly and end collector ceramic collars, respectively.

The two sides of the shield box each have two pairs of through holes, with clearance for socket-head cap screws to secure the RF resistors. Two vertical tapped through holes at the sides and two vertical through holes at the back are used to align and secure the shield box coverplate and patch panel.

Laser-cut mica sheets between the shield box and the heat shield provide additional electrical isolation and prevent the shield box from rotating.

A copper cover-plate traps the grids and RF plates in the shield box. Openings are

provided for wires connected to the grids, RF plates, and end collector. The shield box cover plate is in mechanical and electrical contact with the top edge of the shield box, which is not flame-sprayed.

Wires from the slit, grids, rf plates, end collector, and Langmuir probes lead to male SMA connectors (not shown in Fig.5) which are screwed into an aluminum-oxide coated aluminum patch panel. The patch panel is screwed to the shield box with two socket-head cap screws; additional alignment is provided by pins near the rear of the patch panel. The patch panel allows the omegatron head to be assembled and checked out before being mounted on the tube adapter piece. Semi-rigid coaxial cables terminated with SMA connectors connect to the patch panel at one end and to SMA vacuum feedthroughs at the other end. The lengths of the two coaxial cables to the RF plates are identical to insure a phase match of RF power arrival at the plates.

The subassembly consisting of the shield box, shield box coverplate, and SMA patch panel is secured to the heat shield with a stainless steel mounting plate and a lock plate. The lock plate has four through holes with clearance for silver-plated vented round-head cap screws. The screws secure the mounting plate and shield box subassembly to the tapped through holes in the heat shield.

IV. ELECTRONICS

Figure 6 shows a block diagram of the RF oscillator and amplifier subsystem. A Wavetek 1062 oscillator provides an RF signal with the appropriate frequency which is amplified by an Amplifier Research 15 watt amplifier and sent to the isolation transformer.

The Wavetek 1062 radiofrequency oscillator has a range from 1 to 400 MHz, of which the range 1–100 MHz is used. It has custom analog electronics which accept separate signals between -5 and $+5$ volts to control the RF power and frequency output from the oscillator. A channel of a BiRa 5910 D/A CAMAC module is used to control the frequency; the 12 bit resolution of the BiRa divided amongst 100 MHz gives 25 kHz frequency resolution. The

custom Wavetek analog electronics also offer signals proportional to the power and frequency to read back the oscillator output.

The Wavetek 1062 features crystal oscillators at 5, 20, and 100 MHz which beat with the oscillator output. A "birdy" circuit rectifies and low-pass filters the beat signal, and the output is used to confirm when the oscillator frequency passes over a crystal frequency. The output of the RF oscillator is sent to an Amplfier Research 15 watt wideband RF amplifier, which has a variable gain between +23 and +48 dB selectable with a dial. The amplifier can be switched on or off remotely via CAMAC.

The amplified RF power is applied evenly to both plates using a custom 1:2 isolation transformer; Fig.3 shows a schematic. The RF transformer consists of two parts. The first section converts $50\,\Omega$ input to two balanced $50\,\Omega$ outputs which are 180 degrees out of phase and mirror-symmetric with respect to the input ground. The second section communicates with the first section through DC blocking capacitors and allows the "RF null potential", that is the DC potential at the center of the RF plates, to be set independently. Low level currents resulting from ion collection are extracted at the center tap of the output stage. This technique minimizes the RF leakage into the low-level current detection electronics.

A BiRa B5910 D/A module programs the omegatron analog electronics that supply the bias voltage of the RF plates. This bias is also applied to the case of the isolation transformer. The resonant ion current is collected through a center-tap of the transformer and is sent to the RF ammeter circuit, whose output is digitized.

The RF plate electronics measure nanoampere level currents with up to 200 volts common mode rejection. Each of the three grids, the centertap of the RF transformer, and the end collecter have identical ammeter electronics board layouts. Each board has outputs corresponding to three stages of gain, $\times 1, \times 10$, and $\times 100$, to improve dynamic range. All boards except the RF board have input impedances as low as practical to reduce the voltage fluctuations of the grid/collector that result from fluctuating current arriving at that component. This reduces displacement currents on the RF plates induced by capacitive coupling with adjacent components. All electronics boards have inductors on signal inputs to filter

RF noise. The inductors on the input of the RF card form part of a three-pole LC filter with one capacitance determined by the semi-rigid coaxial cables to the RF plates. Component values are chosen to form a low-pass filter with the -3 dB point set at 15 kHz.

An electrical schematic of the RF ammeter circuit is shown in Fig.7. The current signal is converted to a voltage by amplifier U1 with gain of 10^6 V/A. The current signal from the analogous component of a "virtual omegatron" is converted to a voltage by amplifier U2 and the difference between these voltages is amplified by U3 and U4. The "virtual omegatron" is a network of capacitors whose values are chosen to mimic the capacitive coupling between the real omegatron components. The "virtual omegatron" was not used while collecting the data for this paper, and the input to amplifier U2 was left open. Potentiometers at the inputs of amplifiers U3 and U4 permit balancing of resistor bridges that provide 200 V common mode rejection. The gain of amplifier U4 is set a factor of ten higher than the gain of amplifier U3. The $\times 1$ and $\times 10$ signals are low-pass filtered and buffered. The filtered unbuffered $\times 10$ signal is put through a second buffer with another gain of ten. Optionally, a high bandwidth voltage follower allows the $\times 10$ full band-width signal to be monitored. All output signals are digitized.

Amplifiers U1 and U2 have an isolated ground plane, the potential of which is set to the component bias. The ground plane is connected to the outer shield of the input cables. This is to minimize voltage differences between the center conductor and shield of the input cables thereby reducing leakage currents at high DC bias and displacement currents from cable capacitance during swept bias operation. The isolated ground plane can be driven from -100 volts to $+200$ volts. Each electronics board has a circuit to drive the isolated ground plane voltage, a diagram of which is shown in Fig.8. The desired voltage of the isolated ground plane divided by forty is sent to the differential input of amplifier U13. The option exists to add a unity-gain signal to the desired ground plane voltage using amplifier U14. The final isolated ground plane voltage is also divided by forty with a buffer and digitized.

V. THEORY OF OPERATION

A. Ion Transmission Through Slit and Grids

Ions which have pitch angle greater than the angle defined by the slit or grid aperture can be assumed to have "optical" probability of transmission, i.e. the probability depends only on the relative area of the aperture. When this criterion is applied to a population of ions whose velocity distribution is described by a half-Maxwellian shifted forward in parallel velocity, the slit and grid transmission factors can be computed by taking the ratio of transmitted and incident ion fluxes. In this case, the ion transmission factor through the slit depends on the thickness of the knife-edge and the angle, but in general the transmission factor increases as the distribution is shifted forward, i.e. if the ions are accelerated before entering the slit. For the geometry of our slit the ion transmission factor is estimated to be 20%–30% of optical for an unshifted half-Maxwellian distribution. The transmission factor increases by a factor of two if the distribution is accelerated through a potential equal to twice the ion thermal energy.

The same calculations show that almost full optical transmission of ions can be expected through the grids. Plasma tests demonstrate ion grid transmission of 66% which is close to the optical value of 71%, as expected.[12]

B. Beam Collimation, Space Charge

Ions transmitted through the slit form a non-neutral, collimated ribbon-shaped beam. For sufficiently high currents, space charge can cause the beam both to expand and to reflect low energy ions back to the slit.

Brillouin[13] first pointed out in 1945 that a non-neutral column of charged particles will remain confined by a magnetic field up to a space-charge limit set by the column charge density and the magnetic field strength. The maximum charge density that can be obtained in an equilibrium configuration occurs when $n = n_B \equiv 2\epsilon_0 B^2/m_i$, the Brillouin density.[14,15] For

deuterons in a magnetic field of approximately 5 T, the Brillouin density is $n_B \approx 3\times10^{16}\,\mathrm{m}^{-3}$. Taking the average parallel ion energy to be $\approx 3\,\mathrm{eV}$ (corresponding to the measured value of the ion temperature, see Section VI A), and the cross-section of the beam equal to the slit area, the Brillouin density will be approached when $I \approx 15\,\mu\mathrm{A}$. Thus in order to avoid beam broadening from space charge, the omegatron should be operated with ion currents less than $I \approx 15\,\mu\mathrm{A}$.

The current level at which space charge can cause a significant fraction of the ions to be reflected from the electrostatic self-potential can be computed as follows. The charge density may be related to the beam current as above. The Poisson equation can be solved analytically in between the grids and in the RF cavity for constant charge density, i.e. when the electrostatic potential has a negligible effect on the ion motion. The current limit may be estimated by computing the beam current for which the maximum electrostatic self-potential is of order the ion energy.

For the case when the beam width is much bigger than both the beam thickness ($2c$) and the beam length ($2a$), the maximum self-potential at the center of the beam is[12]

$$\phi_{\max} = \frac{a^2\rho}{2\epsilon_0}\left[1 - \exp\left(\frac{-\pi c}{2a}\right)\right],$$

where ρ is the charge density. For deuterons with $T_i \approx 3\,\mathrm{eV}$, a limiting current of $I \approx 21\,\mu\mathrm{A}$ is estimated for the region between RFEA grids. Thus, in order to avoid ion reflection from space charge in the RFEA, the omegatron should be operated with $I < 21\,\mu\mathrm{A}$.

C. Retarding Field Energy Analysis

The temperature of the electrons or bulk plasma ions can be extracted from the IV characteristic in the standard way:[16] for a flux Γ_s of ions with a half-Maxwellian distribution of velocities at the sheath edge, the fraction that is collected downstream is equal to

$$\frac{\Gamma}{\Gamma_s} = \begin{cases} 1 & \phi_{\max} \le \phi_s, \\ \exp\left(\dfrac{q(\phi_s - \phi_{\max})}{kT}\right) & \phi_{\max} \ge \phi_s, \end{cases}$$

where ϕ_s is the sheath potential and $\phi_{\max}$ is the maximum potential in the analyzer, set by reflector grid bias when space charge is negligible. Thus by sweeping out the reflector grid bias and measuring the current downstream it is possible to extract the distribution temperature.

D. Omegatron Ion Mass Spectrometer

An electric field with amplitude E and frequency ω is applied across the RF cavity. The Larmor radius for ions entering the RF cavity on axis increases according to[4,10,12]

$$r_L(t) = \frac{qE}{m}\frac{\sin((\omega_c-\omega)t/2)}{\omega(\omega_c-\omega)} \approx \frac{Et}{2B},$$

where $\omega_c = qB/m$ is the ion cyclotron frequency and $(\omega_c - \omega)t \ll 1$ is the condition for resonant ions. A simple model predicts that resonant ions are collected on the RF plates if the dwell time in the RF cavity exceeds the time required for the Larmor radius to increase to half the plate spacing (the spin-up time) $\tau = BD/E$, which depends only on the RF plate spacing D, the ambient magnetic field magnitude B, and the amplitude of the applied RF electric field $E = \sqrt{PR}/(D/2)$, but on neither the ion mass nor charge. Here P is the rms power delivered to the RF load and $R = 50\,\Omega$. Resonant ions enter the RF cavity with a distribution of parallel energies, and slowing the distribution, either by externally applied grid bias or internally generated space charge potentials, increases the fraction of the distribution that is collected. The absolute current of resonant ions can be increased by increasing the total current in the RF cavity, but it is found that for total current above $I \approx 10\,\mu$A some ions are reflected back towards the slit, presumably by space charge at the entrance to the RF cavity.

Space charge can also influence the motion of the ions perpendicular to the magnetic field. In Brillouin flow, the angular frequency of the ion orbit, $\omega_{\rm res}$, is down-shifted by an amount that depends on the charge density of the beam. Characterizing the beam density in terms of the plasma frequency, $\omega_p^2 = q^2 n/(\epsilon_0 m)$, the down shift is

$$\omega_{\rm res} - \omega_c \approx -\frac{\omega_p^2}{2\omega_c},$$

for $\omega_p^2/\omega_c^2 \ll 1$. Thus, for a fixed average velocity of the beam, the down-shift would be roughly proportional to the beam current.

A kinetic model of resonant ion collection in the RF cavity has been developed which incorporates physics that has been demonstrated to be important in the operation of the omegatron.[12] The model considers a shifted half-Maxwellian distribution for parallel ion velocities and computes the portion of this distribution that has sufficient dwell-time in the cavity to be collected on the RF plates. The model accounts for ions being reflected near the entrance of the RF cavity by space charge and assumes that the potential structure along the beam in the RF cavity is mostly flat. The latter assumption is consistent with the 3-d potential distribution that solves Poisson's equation for the case of a constant density beam. A result of the model is a relationship between the collected resonant current, $I_{\rm RF}$, the flux of resonant impurity ions at the sheath edge, Γ_s, the spin up time τ, and the temperature of the impurity ions, T,

$$I_{\rm RF} = qA\xi^3\xi_s\Gamma_s \exp\left(\frac{-q\phi_0}{kT}\right)\left[1 - \exp\left(\frac{-m(L/\tau)^2}{2kT}\right)\right].$$

Other factors in this equation are listed as follows: A is the ion beam area, ξ is the transmission factor of the grids, ξ_s is the transmission factor for the slit, ϕ_0 is the maximum electrostatic potential in the RF cavity, and L is the RF cavity length. Note that the spin-up time, $\tau = BD/E$, is related to the RF power, $\tau^{-2} \sim P$.

For each identifiable resonance, the amplitude versus applied RF power can be fit by least squares to a function of the form $I_{\rm RF} = c_0[1 - \exp(-P/c_1)]$. The ratio of impurity temperatures T and impurity mass m for each resonance is obtained from the fitting coefficient c_1. Dividing the resonant current by the non-resonant current, the beam area and transmission factors cancel, and the impurity flux fractions $\Gamma_s/\Gamma_{\rm bulk}$ can be found from the fitting coefficients $c_0 = I_{\rm RF}$,

$$\frac{kT}{m} = c_1\frac{2L^2R}{B^2D^4}, \qquad \frac{\Gamma_s}{\Gamma_{\rm bulk}} = \frac{(I_{\rm RF}/q)}{(I_{\rm END}/q_{\rm bulk})}\frac{\exp[(-q_{\rm bulk}\phi_0)/kT_i]}{\exp[(-q\phi_0)/kT]}.$$

Here, I_{END} refers to the current collected on the end collector, T_i is the bulk ion temperature, and q, q_{bulk} are the charges on the resonant impurity and bulk ion species, respectively.

The potential ϕ_0 in the analyzer can be estimated[12] from the fraction of bulk plasma current arriving on the grids as follows: The grid biases can be set to ensure no ions are reflected inside the analyzer (i.e. resulting in maximum transmission to the end collector), and the currents measured on all components can be used to determine the grid transmission factors, ξ. With the grid transmission factors known, current collected in excess of $1-\xi$ can be attributed to reflection from space charge potentials. By assuming a shifted, half-Maxwellian bulk ion distribution in the analyzer, the magnitudes of the reflecting potentials due to space charge can be estimated.

Particle orbit theory predicts the resonance frequency width comes from a convolution of at least three effects:[12] finite geometric size of the omegatron, $\Delta\omega_{\mathrm{res}} = EB/D$, magnetic field variation, $\Delta\omega_{\mathrm{res}} = \omega_c \Delta B/B$, and Brillouin flow broadening, $\Delta\omega_{\mathrm{res}} = \Delta(\omega_p^2)/(2\omega_c)$, where $\Delta(\omega_p^2)$ is due to fluctuations in the charge density in the RF cavity, caused by fluctuations in Γ_{bulk}. The magnetic field variation comes mostly from the decrease of toroidal magnetic field over the major radial extent of the omegatron slit. The observed widths for resolved and unique resonances are between one and two times the total width predicted by theory.

VI. EXPERIMENTAL RESULTS

A. Retarding Field Energy Analysis

The grids and end collector of the omegatron probe can be operated as a retarding field energy analyzer. Figure 10 shows a typical ion current-voltage characteristic from a typical Alcator C-mod discharge (deuterium plasma, toroidal field $B = 5.1\,\mathrm{T}$, plasma current $I_p = 1.0\,\mathrm{MA}$, line-averaged core density $n_e = 10^{20}\,\mathrm{m}^{-3}$, core electron temperature $T_e = 1.1\,\mathrm{keV}$, ohmically heated). For the time range indicated in Fig.10 the omegatron Langmuir probes obtained measurements on flux surfaces between $37 \leq \rho\,[\mathrm{mm}] \leq 39$ outside the separatrix

(mapped to the outer midplane), where the plasma density is $4 \times 10^{16} \leq n_e\,[\mathrm{m}^{-3}] \leq 2 \times 10^{17}$ and the electron temperature is $T_e \approx 5\,\mathrm{eV}$. Biases of components were set as in Fig.9, with grid G2 as parallel energy selector. The floating potential, ϕ_f in Fig.10, is measured with Langmuir probe LP2. The knee potential ϕ_k is extracted from the IV characteristic graphically as shown.

As shown in Fig.10, the knee potential is typically found to be more negative than the floating potential. This is believed to be caused by the presence of space charge inside the analyzer. Space charge can contribute to the electrostatic potential such that the reflector bias is lower than the maximum potential experience by ions in the analyzer. Analysis shows[12] that space charge can significantly influence the shape of the IV characteristics for voltages near the sheath potential bias when currents are greater than $I \approx 10\,\mu\mathrm{A}$, as shown in Fig.10. It is typically found that the ion distribution function can be described by a two-temperature distribution, with a cold majority and a hot minority. These results suggest that the majority of deuterium ions collected at the omegatron are formed by ionization of cold neutrals evolving off wall surfaces.[12]

B. Ion Mass Spectrum

Figure 11 shows an impurity spectrum obtained during an Alcator C-Mod discharge with similar parameters as given above. The signal to the RF plates has been digitally filtered and normalized by the non-resonant current to the end collector. The noise floor for the digitally filtered, normalized signal is $I_{\mathrm{RF}}/I_{\mathrm{END}} \approx 5 \times 10^{-4}$. The grid biases for omegatron ion mass spectrometer mode are set as in Fig.12 to maximize the dwell time for bulk of the resonant ion distribution, including the influence of space charge in the RF cavity.

In deuterium plasma, the dominant resonance is at $M/Z = 2$, and the $M/Z = 4$ resonance is often present. Resonances are observed at charge to mass ratios M/Z which correspond to the charged states of the following isotopes: ^{10}B, ^{11}B, ^{12}C, ^{14}N, and ^{16}O. Other resonances, some of which are not shown in Fig.11, have been observed to increase

when impurity gases have been puffed. For instance, puffing H_2, ^{3}He, ^{4}He, or N_2 results in an increase in the appropriate resonances corresponding to $^1H^+$, $^3He^+$, $^3He^{2+}$, $^4He^+$, $^{14}N^{2+}$ or $^{14}N^{3+}$. The resonances corresponding to the charged states of boron appear in approximately the same proportions as the isotopic abundances (19.9% ^{10}B, 80.1% ^{11}B). For $M/Z > 12$ the resonances are not well resolved.

C. Noise

Figure 13 shows the ambient noise power spectrum recorded on the omegatron RF plates without plasma, with plasma but the omegatron withdrawn, and with plasma and the omegatron inserted. In absence of plasma the noise floor of the RF ammeter electronics is at level of a few CAMAC bits on the $\times 100$ gain channel, equivalent to a current of $I_{\mathrm{RF,noise}} \approx 0.02\,\mathrm{nA}$ RMS. Harmonics can be seen, probably acoustic coupling to vacuum pump vibrations. With the omegatron inserted into plasma, the noise floor increases by more than three orders of magnitude, to equivalent current $I_{\mathrm{RF,noise}} \approx 20\,\mathrm{nA}$ RMS. The noise spectrum in the bottom panel of Fig.13 increases with frequency beyond one kilohertz; the decrease of power beyond 15–17 kHz in the noise spectrum is due to the roll-off of the LC filter on the input of the ammeter electronics.

The present design of the omegatron has the slit electrically connected to the box surrounding the RF cavity; an unintentional consequence is around 30 picofarads capacitive coupling between the RF plates and the slit. Therefore fluctuating voltage on the slit induces a current on the RF plates. The slit typically receives plasma current that fluctuates with large amplitude and a broad power spectrum. If the impedance of the slit to ground is high, the fluctuating current produces a large fluctuating voltage. To reduce this effect the input impedance of the slit ammeter electronics is set as low as possible, around $0.5\,\Omega$. A more effective solution would be to break the capacitive coupling between the RF cavity and the slit altogether, which requires electrically isolating the slit from the shield box. This could potentially reduce the noise on the RF plates by an order of magnitude.

Synchronous detection also could be employed to improve signal-to-noise. Electronics have been constructed and successfully demonstrated to modulate the RF power at 10 kHz and to synchronously detect the resultant signal. However, this technique has not been employed presently owing to the large noise component at 10 kHz during plasma operation (see bottom panel of Fig.13). If the capacitive coupling of the RF plates to the plasma fluctuations can be significantly reduced, this technique may become advantageous as it would avoid the low frequency acoustic coupling noise in the present system.

Simple digital signal filtering (binning) reduces the noise by a factor of five or more, which improves the signal-to-noise. We exploit the theoretical predictions for the frequency width to remove much narrower features in the M/Z spectrum caused by noise. For instance, typical resonance width is expected to be 0.3 MHz, considering just intrinsic single-particle resonance convolved with magnetic field variation, so the binning width is chosen to be 0.25 MHz. For monotonically swept frequencies the binning procedure is essentially a boxcar average. Filtering by convolution with a Savitzky-Golay kernel[17] gives similar results. The binning technique can also be used with periodic signals which change linearly in time, say multiple sweeps over the same frequency range, to reduce portions of the signal from different time periods which do not correlate; this amounts to a histogram.

In practice the quantity we are interested in is the fraction of plasma arriving at the omegatron corresponding to each impurity species. A simple way to remove the gross effects of plasma fluctuations is to divide the resonant RF current by the non-resonant end current, as shown in Fig.11.

D. Resonance Frequency, Amplitude

Figure 14 shows the center frequency of the $M/Z = 4$ resonance as a function of the non-resonant current arriving at the end collector. The center frequency of the resonance has the expected dependence on the non-resonant current (see Section V D), approaching the cyclotron frequency at zero current and shifting below the cyclotron frequency at high

non-resonant current.

Figure 15 shows the resonance amplitude as a function of applied RF power for the $M/Z = 4$ resonance. The amplitude of the resonance vanishes at zero applied RF power, increases with applied RF power, and reaches a saturation value as indicated in Fig.15. This behavior is expected from a simple particle collection theory (see Section V D).

E. Impurity Temperatures and Fluxes

A mosaic of the ion impurity spectrum from $3 < M/Z < 12$ was obtained at several different applied RF powers during a sequence of plasma discharges, with the idea to infer the impurity temperature and relative impurity concentrations, using the methods outlined in Section V D.

The impurity densities in the plasma can be obtained from the fluxes by assuming a value of the impurity flow velocity at the sheath edge. For the plasmas studied here, the impurities experience a number of collisions with the bulk plasma ions in the presheath, thus they have the same flow velocity at the sheath edge as the bulk ions. In this case, the impurity density fraction is equal to the impurity flux fraction. The results of temperature and impurity flux fraction analysis are shown in Fig.16. Impurity temperatures are all between 2–3 eV, within the uncertainties of the fits. These temperatures are consistent with what one would expect in a collisional plasma where $T \approx T_{\rm bulk}$. The qualitative features of the flux fractions can be recognized in the raw impurity spectrum, Fig.11. The calculated impurity flux fractions are all below three percent, with $M/Z = 4$ ($^2H_2^+$) and $M/Z = 11$ ($^{11}B^+$) the largest.

F. Residual Gas Analysis

By a simple change of bias to the grids, the omegatron can be operated as a residual gas analyzer, in-situ in the scrape-off layer plasma. The grid biases are set to reject plasma ions and to accelerate plasma electrons into the RF cavity; ions formed in the RF cavity by electron impact are collected with the ion mass spectrometer. Figure 17 shows the ion

spectrum obtained from operating the omegatron as a residual gas analyzer. The resonance at $M/Z = 4$ is dominant, and the resonances with the next highest amplitudes are lower by a factor of five with $M/Z = 3, 2$. Several other resonances are observed, but note the resonance spectrum is completely different from the plasma ion spectra.

Using tabulated cross sections and the known electron energy it is possible to infer the neutral gas pressure inside the omegatron. A lower bound for the neutral molecular deuterium density n_0 can be obtained from $n_0 \geq (I_{\mathrm{RF}})/(I_e \sigma_{\max} L)$, where I_{RF} is the resonant singly-ionized molecular deuterium current collected, I_e is the electron current to the end collector, L is the RF cavity length, and $\sigma_{\max} = 10^{-16}\,\mathrm{cm}^2$ is the maximum cross section (which occurs at 60 eV) for ionization of molecular hydrogen by electron impact.[18] Assuming the molecular deuterium is at the wall temperature gives the pressure. It should be noted that the omegatron cavity in Alcator C-Mod is not designed at present to communicate well with neutrals outside the analyzer. Thus the neutral density inside the analyzer is typically $n_0 \approx 6 \times 10^{18}\,\mathrm{m}^{-3}$, such that on average, ions suffer much less than one ion-neutral collision while passing through the RFEA or IMS cavities.

VII. CONCLUSIONS

A probe combining an omegatron ion mass spectrometer with a retarding field energy analyzer has been commissioned on the high-field Alcator C-Mod tokamak. This spectrometer extends ion mass spectrometry to high-field regimes with $B > 4\,\mathrm{T}$. Special vacuum hardware construction and electronics design techniques are described. A spectrum of ion impurities with $M/Z < 12$ has been obtained, and the amplitudes and widths compared with theory. Sources of noise are discussed and modifications to the vacuum hardware to reduce noise are suggested. From the variation of the amplitudes with applied RF power the temperatures and absolute fluxes of individual ion impurity species have been obtained. In addition, operation of the omegatron probe as an in-situ residual gas analyzer is demonstrated.

Acknowledgements

The authors would like to thank Prof. Ian Hutchinson and Drs. Earl Marmar, Peter Stangeby and Garry McCracken for guidance and support. Special thanks are extended to Dr. Kevin Wenzel, Jerry Hughes, Khash Shadman, and Imad Jureidini for their contributions to the hardware. The excellent work is acknowledged of Dave Gilbert at DCM Machine for machining most of the intricate omegatron components, and Elliot Goldman at Communication Coil for assembling the RF isolation transformers. Work supported by the MIT Nuclear Engineering Department and D.o.E. Coop. Agreement DE-FC02-99ER54512.

REFERENCES

[1] P. Stangeby and G. McCracken, Nuclear Fusion **30**, 1225 (1990).

[2] G. Matthews, Plasma Physics and Controlled Fusion **31**, 841 (1989).

[3] I. Hutchinson *et al.*, Physics of Plasmas **1**, 1551 (1994).

[4] J. Hipple, H. Sommer, and H. Thomas, Physical Review **72**, 1877 (1949).

[5] D. Alpert and R. Buritz, Journal of Applied Physics **25**, 202 (1954).

[6] J. Wagener and P. Marth, Journal of Applied Physics **28**, 1027 (1957).

[7] A. Averina, G. Levina, V. Lepekhina, and A. Rafal'son, Pribory i Tekhnika Éksperimenta 121 (1964).

[8] E. Wang, L. Schmitz, B. LaBombard, and R. Conn, Review of Scientific Instruments **61**, 2155 (1990).

[9] T. Mieno, H. Kobayashi, and T. Shoji, Measurement Science and Technology **4**, 193 (1993).

[10] E. Thomas Jr., Master's thesis, Massachusetts Institute of Technology, 1993, Technical Report No. PFC/RR-93-3, MIT Plasma Fusion Center, Cambridge, MA.

[11] A. Wan, T. Yang, B. Lipschultz, and B. LaBombard, Review of Scientific Instruments **57**, 1542 (1986).

[12] R. Nachtrieb, Ph.D. thesis, Massachusetts Institute of Technology, 2000, Technical Report No. PSFC/RR-00-2, MIT Plasma Science and Fusion Center, Cambridge, MA, `http://www2.psfc.mit.edu/library/preprints.html`.

[13] L. Brillouin, Physical Review **67**, 260 (1945).

[14] N. Krall and Trivelpiece, *Principles of Plasma Physics* (San Francisco Press, San Francisco, 1986).

[15] R. Davidson, *Physics of Nonneutral Plasmas*, *Frontiers in Physics* (Addison Wesley, ADDRESS, 1990).

[16] I. Hutchinson, *Principles of Plasma Diagnostics*, 2nd ed. (Cambridge University Press, Cambridge, UK, 1987).

[17] W. Press, S. Teukolksy, W. Vetterling, and B. Flannery, *Numerical Recipes in C*, 2nd ed. (Cambridge University Press, Cambridge, 1992).

[18] R. Janev, W. Langer, K. Evans Jr., and D. Post Jr., *Elementary Processes in Hydrogen-Helium Plasmas* (Springer-Verlag, Berlin, 1987).

FIGURES

FIG. 1. Poloidal cross section of Alcator C-Mod tokamak showing omegatron (mirror image) inserted into upper divertor scrape-off layer plasma. Box around omegatron corresponds to Fig.2. Contours correspond to magnetic flux surfaces in the scrape-off layer plasma. Magnetic field strength at the omegatron location is approximately $B \approx 4.8\,\mathrm{T}$.

FIG. 2. Omegatron probe (mirror image) on Alcator C-Mod tokamak. Representative flux surfaces are shown, spaced two millimeters apart at the midplane.

FIG. 3. Schematic of Omegatron probe, showing slit, retarding field energy analyzer, and ion mass spectrometer portions mounted in a shielding box.

FIG. 4. Exploded view of internal components of omegatron probe retarding field energy analyzer and ion mass spectrometer, showing: slit; grids; RF plates; RF resistors; end collector; mica spacers and insulators; and ceramic spacers and supports. Wires to the grids, RF plates, and RF resistors omitted for clarity.

FIG. 5. Exploded view of external components of omegatron probe, showing: heat shield; shield box; coverplate; patch panel; mounting plate; lock plate; and support plate. All wires and SMA connectors omitted for clarity.

FIG. 6. Block diagram of RF amplifier subsystem.

FIG. 7. Electrical schematic of omegatron RF plate ammeter circuit.

FIG. 8. Electrical schematic of isolated ground plane bias circuit. The potential of the isolated ground plane sets the bias potential of the grid/collector component connected to the ammeter input.

FIG. 9. Schematic cross section of omegatron and axial vacuum potential structure. Configuration with G2 as ion parallel energy selector is shown, with SLIT grounded, $V = 0\,\mathrm{V}$.

FIG. 10. Current-voltage characteristics from the omegatron in retarding field energy analyzer mode, showing processed values of cold and hot ion temperatures and knee potential. Floating potential is obtained from Langmuir probe LP2. Solid line is current to END collector normalized by sum of currents to grids G1, G2, G3, and to END collector, scaled to agree with the raw saturation current, and smoothed with boxcar average 2 volts wide.

FIG. 11. Typical impurity spectrum: ratio of resonant current to non-resonant current as a function of ratio species mass and charge. Annotations near resonances identify the most likely impurity charge states. The signal is digitally binned over regions 0.25 MHz wide, chosen to leave intact features with widths near the expected resonance width.

FIG. 12. Optimized component bias arrangement for omegatron ion mass spectrometer operation. The potential profiles between are not determined by experiment but indicated the likely influence of space charge.

FIG. 13. Omegatron ambient noise spectrum without plasma (top), with plasma but omegatron withdrawn (middle), and with plasma and omegatron inserted (bottom).

FIG. 14. Down-shift of $M/Z = 4$ resonance center frequency as a function of non-resonant current, a clear indication of Brillouin flow effects.

FIG. 15. Normalized resonant ion current versus applied RF power. Solid line is least squares fit of function $y = c_0[1 - \exp(-x/c_1)]$; dotted lines represent the function evaluated with one standard deviation change in both fitted parameters.

FIG. 16. Impurity temperatures and flux fractions at sheath edge, obtained from RF power scan technique for range $3 < M/Z < 12$. Labels identify assumed source of the resonances. Density fractions equal flux fractions, assuming collisional presheath.

FIG. 17. Omegatron residual gas analyzer spectrum of M/Z of ion species formed inside the omegatron by electron impact ionization. Note that $M/Z = 4$ resonance is dominant, probably corresponding to D_2^+.

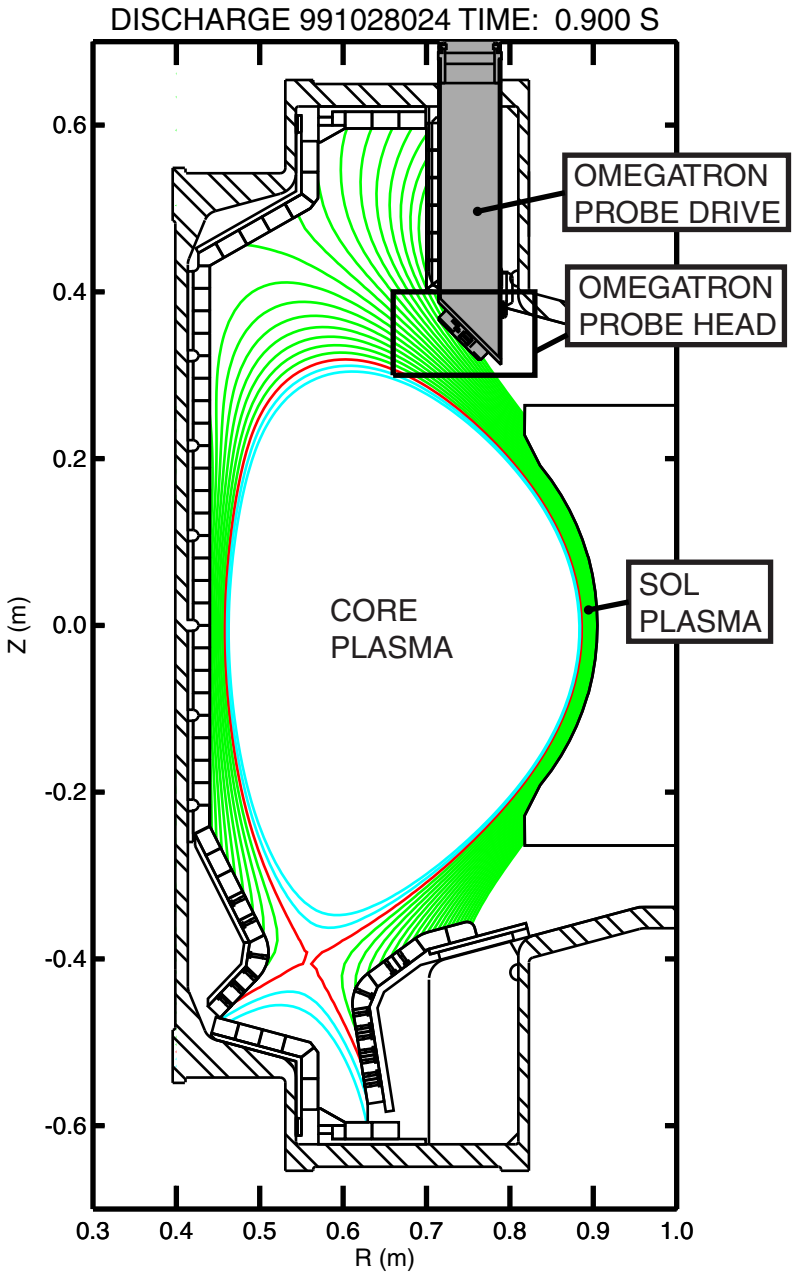
DISCHARGE 991028024 TIME: 0.900 S
OMEGATRON
PROBE DRIVE
OMEGATRON
PROBE HEAD
SOL
PLASMA
CORE
PLASMA
Z (m)
R (m)
0.6
0.4
0.2
0.0
-0.2
-0.4
-0.6
0.3
0.4
0.5
0.6
0.7
0.8
0.9
1.0

FIGURE 01

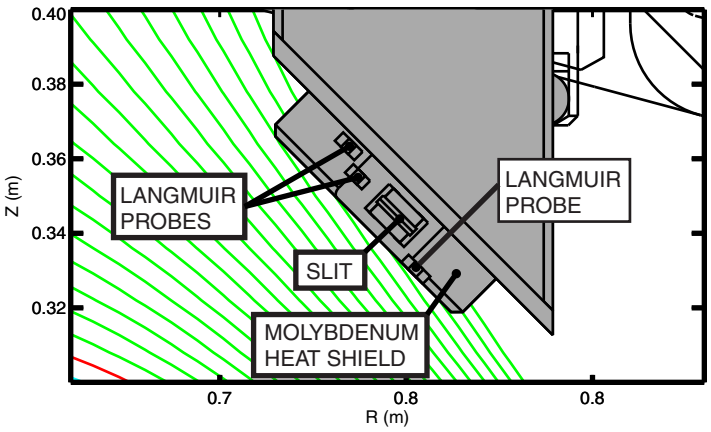
0.40
0.38
0.36
0.34
0.32
Z (m)
0.7
0.8
0.8
R (m)
LANGMUIR
PROBES
LANGMUIR
PROBE
SLIT
MOLYBDENUM
HEAT SHIELD

FIGURE 02

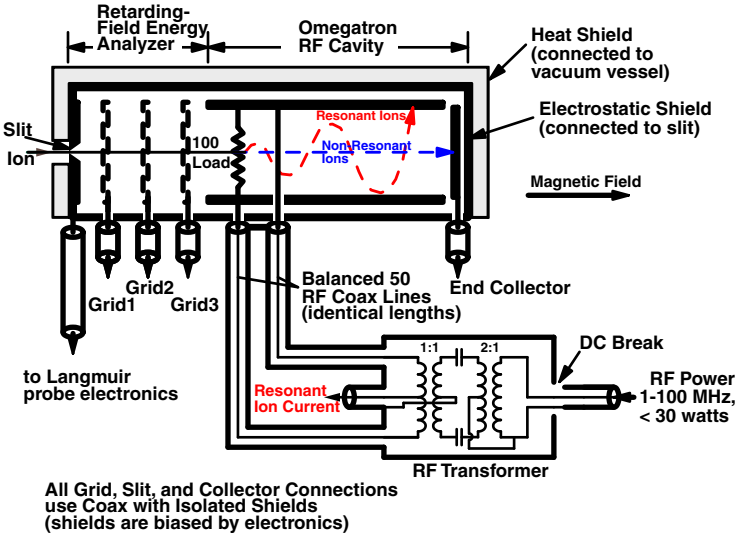
Retarding-
Field Energy
Analyzer
Omegatron
RF Cavity
Heat Shield
(connected to
vacuum vessel)
Electrostatic Shield
(connected to slit)
Slit
Ion
100
Load
Resonant Ions
Non-Resonant
Ions
Magnetic Field
Grid1
Grid2
Grid3
Balanced 50
RF Coax Lines
(identical lengths)
End Collector
DC Break
1:1
2:1
RF Power
1-100 MHz,
< 30 watts
to Langmuir
probe electronics
Resonant
Ion Current
RF Transformer
All Grid, Slit, and Collector Connections
use Coax with Isolated Shields
(shields are biased by electronics)

FIGURE 03

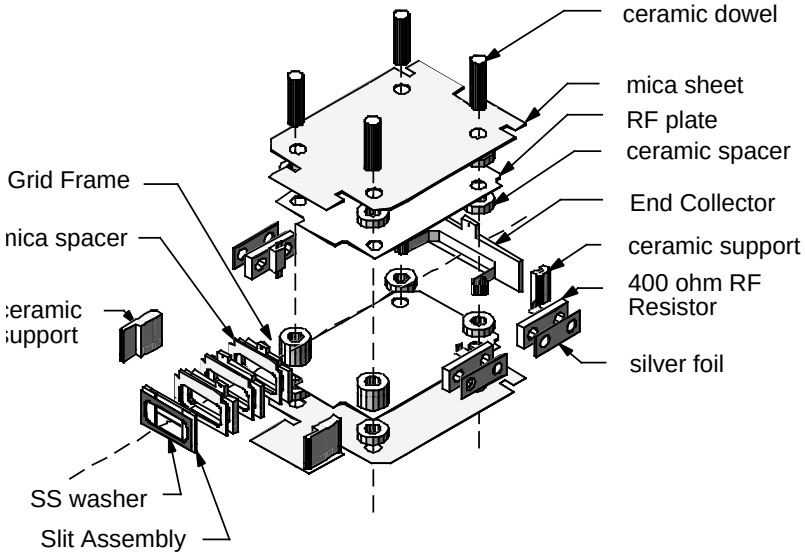
ceramic dowel
mica sheet
RF plate
ceramic spacer
Grid Frame
End Collector
nica spacer
ceramic support
400 ohm RF
Resistor
eramic
upport
silver foil
SS washer
Slit Assembly

FIGURE 04

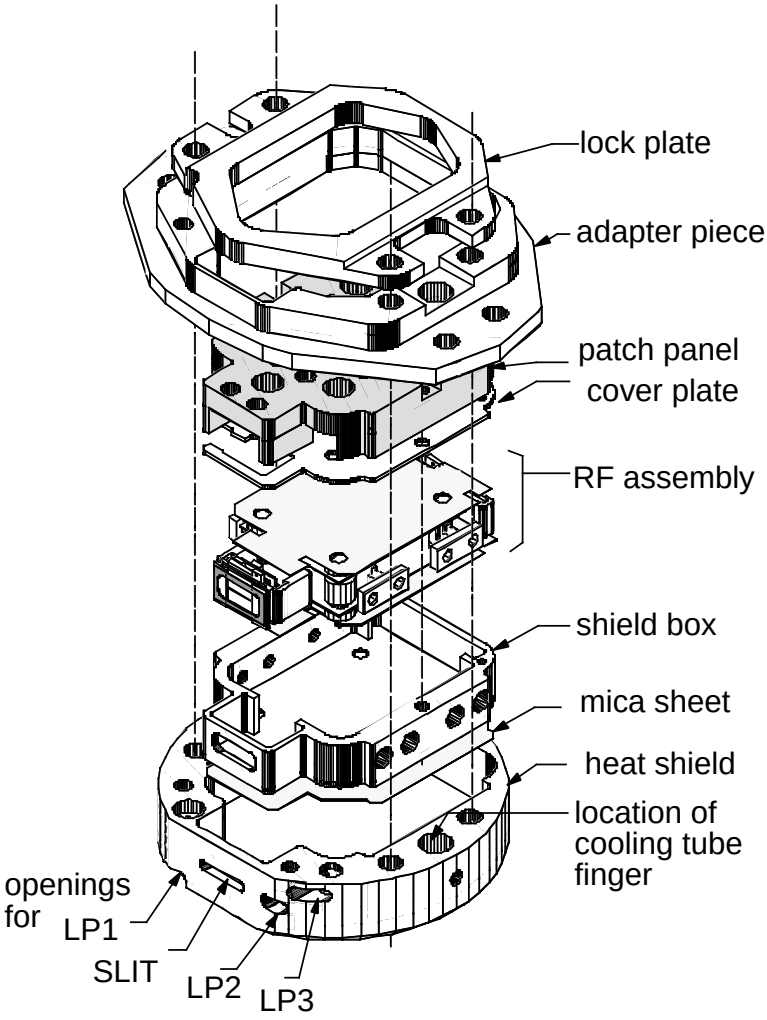
lock plate
adapter piece
patch panel
cover plate
RF assembly
shield box
mica sheet
heat shield
location of
cooling tube
finger
openings
for
LP1
SLIT
LP2
LP3

FIGURE 05

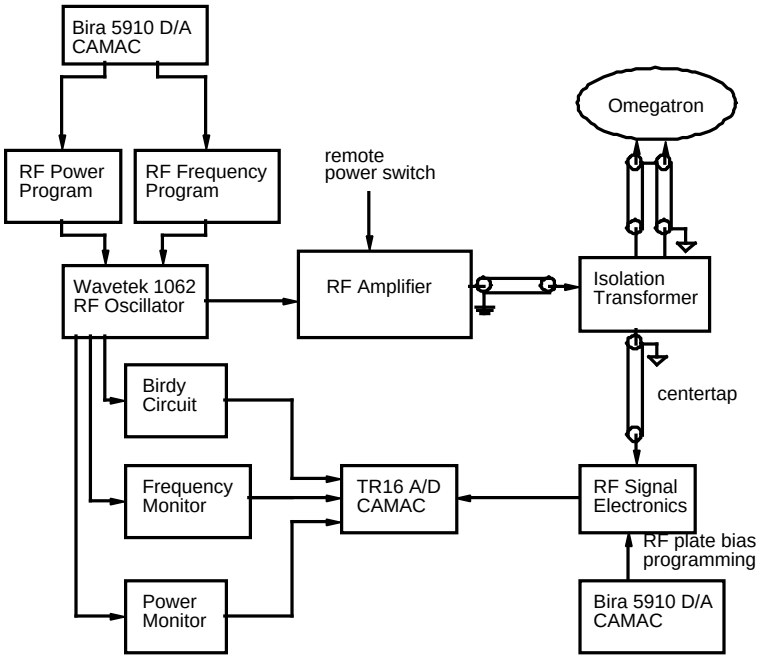
Bira 5910 D/A
CAMAC
RF Power
Program
RF Frequency
Program
remote
power switch
Omegatron
Wavetek 1062
RF Oscillator
RF Amplifier
Isolation
Transformer
Birdy
Circuit
centertap
Frequency
Monitor
TR16 A/D
CAMAC
RF Signal
Electronics
RF plate bias
programming
Power
Monitor
Bira 5910 D/A
CAMAC

FIGURE 06

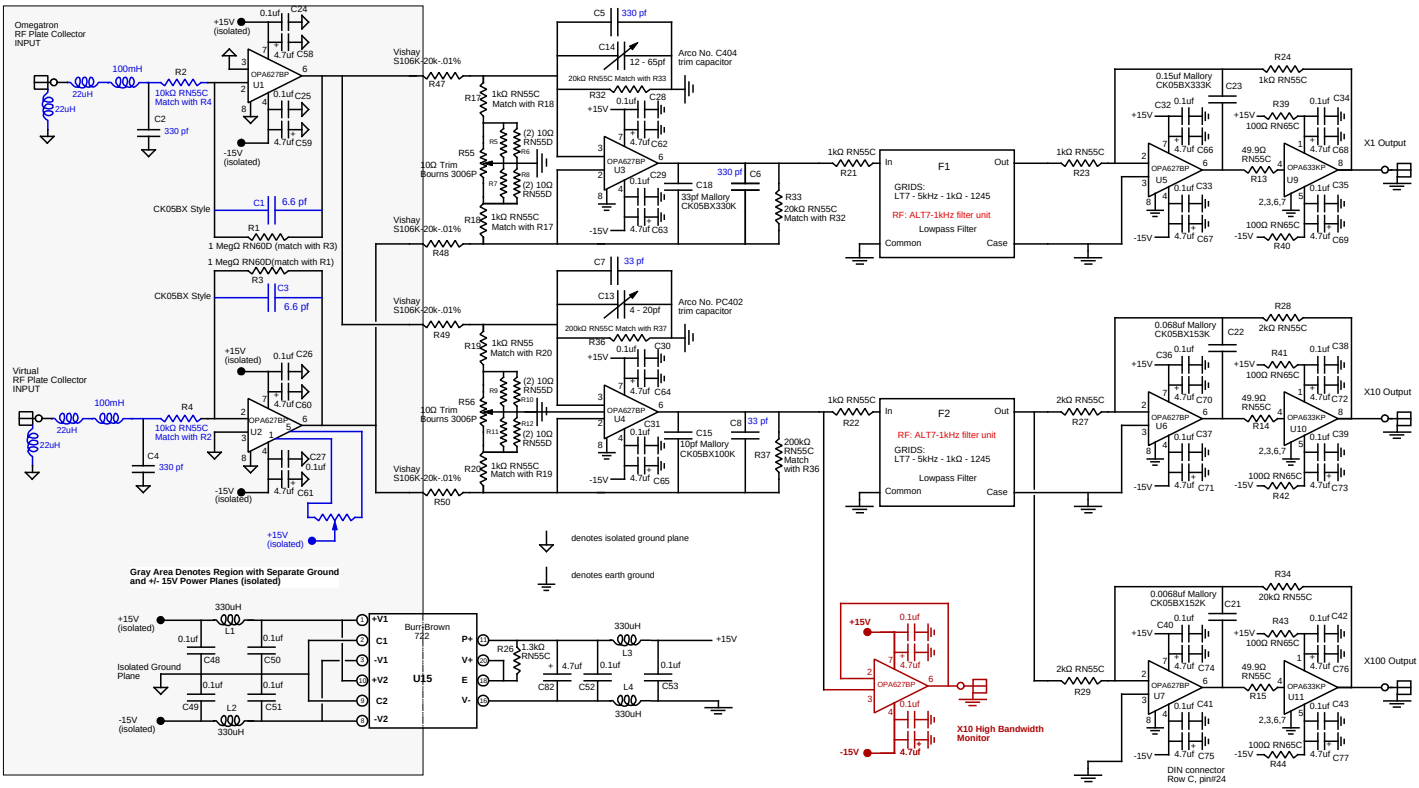
Omegatron
RF Plate Collector
INPUT
Virtual
RF Plate Collector
INPUT
Gray Area Denotes Region with Separate Ground and +/- 15V Power Planes (isolated)
denotes isolated ground plane
denotes earth ground
Isolated Ground Plane
Burr-Brown 722
U15
F1
F2
GRIDS:
LT7 - 5kHz - 1kΩ - 1245
RF: ALT7-1kHz filter unit
Lowpass Filter
Common
Case
X1 Output
X10 Output
X100 Output
X10 High Bandwidth Monitor
DIN connector
Row C, pin#24

FIGURE 07

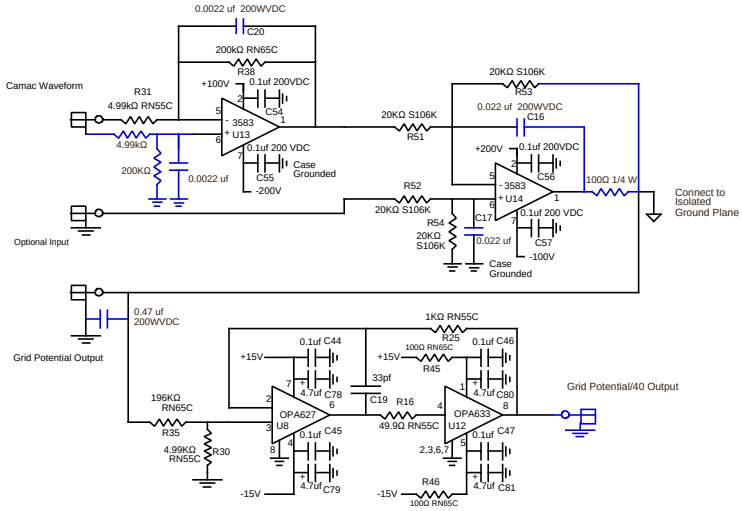
0.0022 uf 200WVDC
C20
200kΩ RN65C
R38
20KΩ S106K
R53
Camac Waveform
R31
4.99kΩ RN55C
+100V
0.1uf 200VDC
C54
3
5
6
- 3583
+ U13
1
20KΩ S106K
R51
0.022 uf 200WVDC
C16
4.99kΩ
200KΩ
0.0022 uf
7
0.1uf 200 VDC
C55
Case
Grounded
-200V
+200V
0.1uf 200VDC
C56
2
5
- 3583
+ U14
1
100Ω 1/4 W
Connect to
Isolated
Ground Plane
R52
20KΩ S106K
6
7
0.1uf 200 VDC
C57
-100V
R54
20KΩ
S106K
C17
0.022 uf
Case
Grounded
Optional Input
0.47 uf
200WVDC
Grid Potential Output
1KΩ RN55C
R25
100Ω RN65C
+15V
0.1uf C44
0.1uf C46
R45
33pf
C19
R16
49.9Ω RN55C
4.7uf C78
4.7uf C80
OPA627
U8
OPA633
U12
Grid Potential/40 Output
196KΩ
RN65C
R35
4.99KΩ
RN55C
R30
0.1uf C45
0.1uf C47
2,3,6,7
-15V
4.7uf C79
4.7uf C81
R46
100Ω RN65C

FIGURE 08

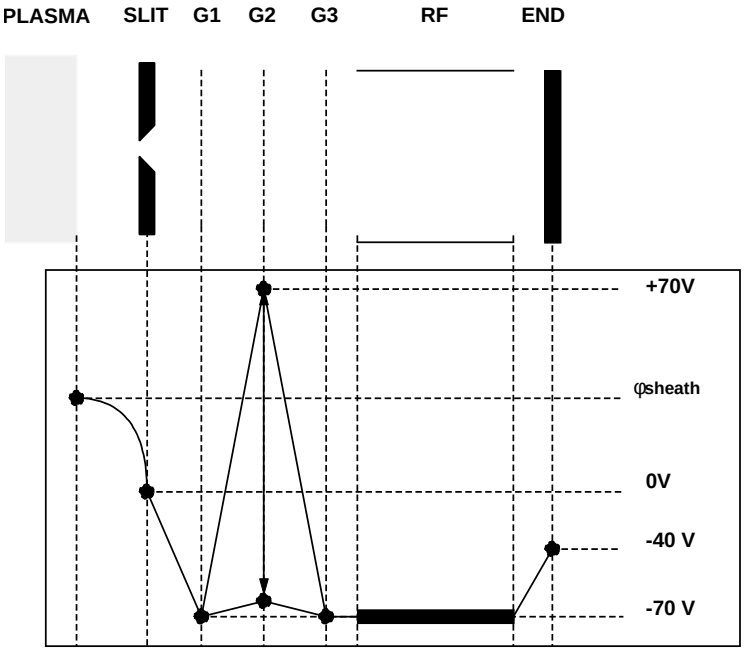

FIGURE 09

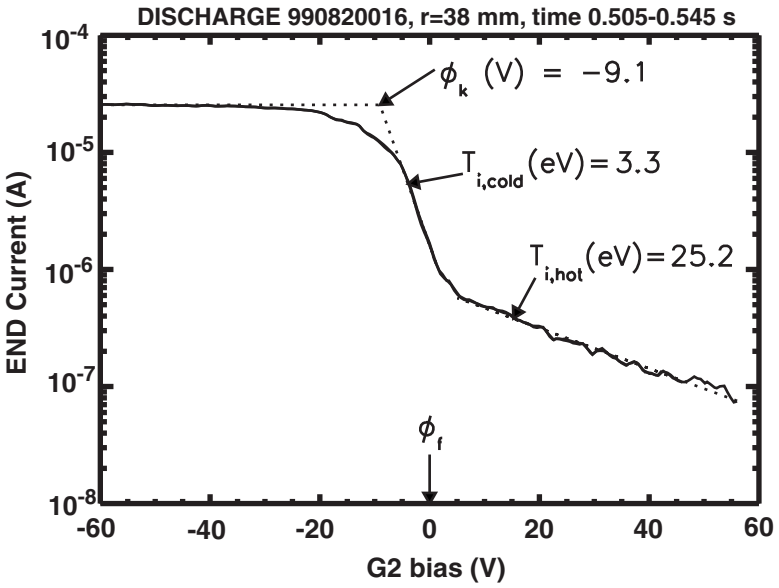
DISCHARGE 990820016, r=38 mm, time 0.505-0.545 s
END Current (A)
G2 bias (V)
ϕ_k (V) = −9.1
$T_{i,cold}$(eV) = 3.3
$T_{i,hot}$(eV) = 25.2
ϕ_f
10^{-4}
10^{-5}
10^{-6}
10^{-7}
10^{-8}
-60
-40
-20
0
20
40
60

FIGURE 10

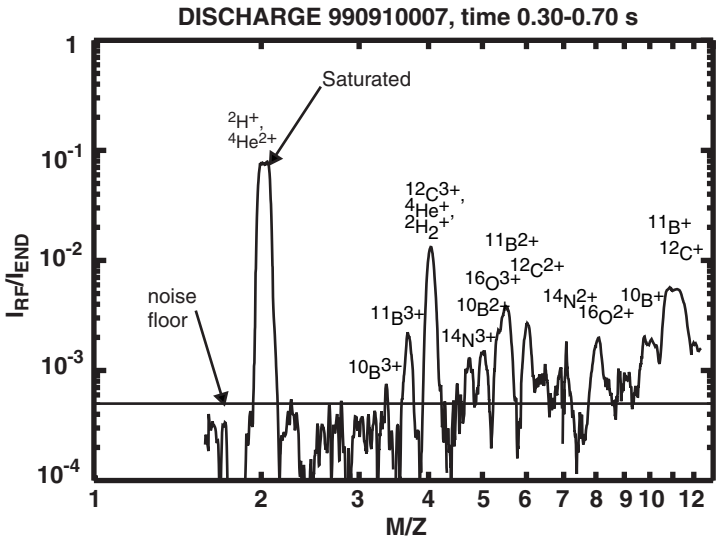
DISCHARGE 990910007, time 0.30-0.70 s
Saturated
$^{2}H^{+}$, $^{4}He^{2+}$
noise floor
$^{10}B^{3+}$
$^{11}B^{3+}$
$^{12}C^{3+}$, $^{4}He^{+}$, $^{2}H_{2}^{+}$
$^{14}N^{3+}$
$^{16}O^{3+}$
$^{10}B^{2+}$
$^{11}B^{2+}$
$^{12}C^{2+}$
$^{14}N^{2+}$
$^{16}O^{2+}$
$^{10}B^{+}$
$^{11}B^{+}$
$^{12}C^{+}$
I_{RF}/I_{END}
M/Z

FIGURE 11

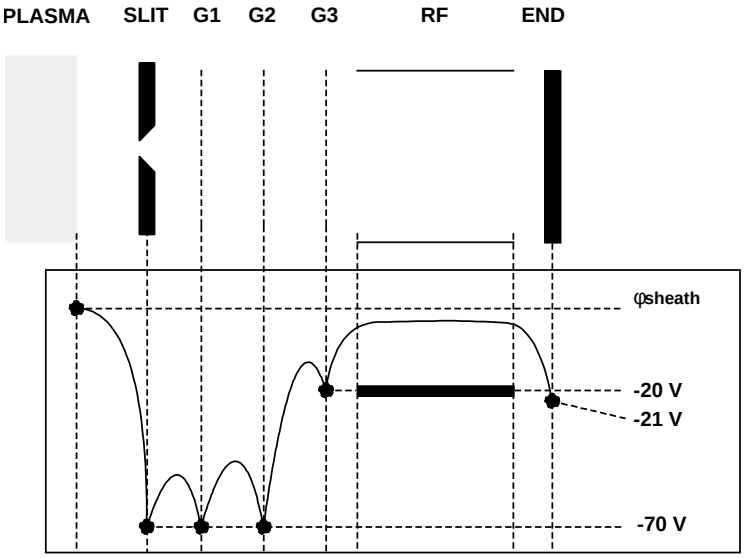

FIGURE 12

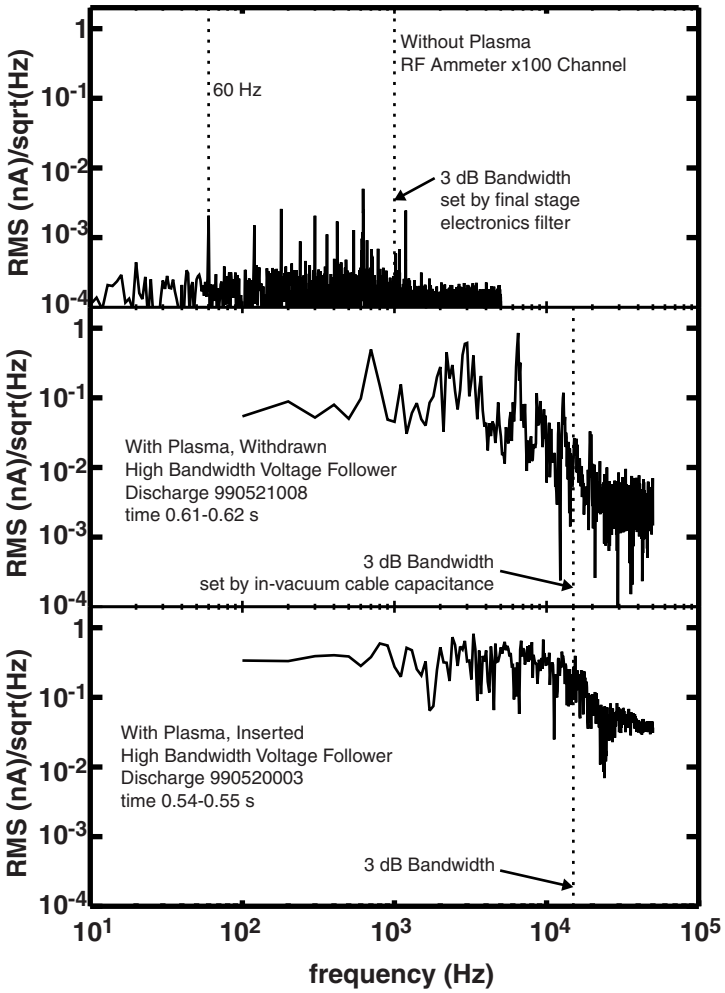
RMS (nA)/sqrt(Hz)
1
10-1
10-2
10-3
10-4
60 Hz
Without Plasma
RF Ammeter x100 Channel
3 dB Bandwidth
set by final stage
electronics filter
With Plasma, Withdrawn
High Bandwidth Voltage Follower
Discharge 990521008
time 0.61-0.62 s
3 dB Bandwidth
set by in-vacuum cable capacitance
With Plasma, Inserted
High Bandwidth Voltage Follower
Discharge 990520003
time 0.54-0.55 s
3 dB Bandwidth
10^1
10^2
10^3
10^4
10^5
frequency (Hz)

FIGURE 13

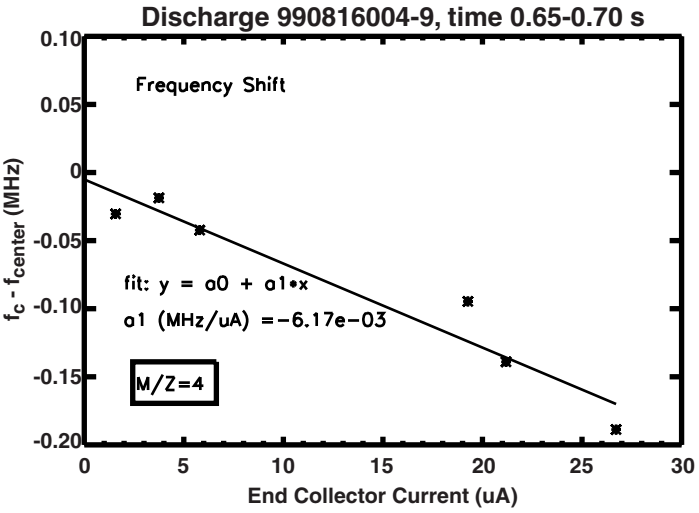
Discharge 990816004-9, time 0.65-0.70 s
Frequency Shift
fit: y = a0 + a1•x
a1 (MHz/uA) =-6.17e-03
M/Z=4
$f_c - f_{center}$ (MHz)
End Collector Current (uA)
0.10
0.05
0
-0.05
-0.10
-0.15
-0.20
0
5
10
15
20
25
30

Figure 14

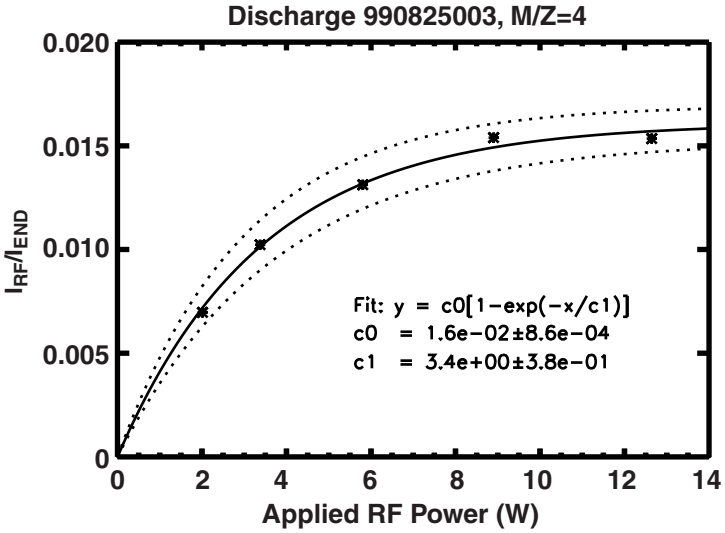
Discharge 990825003, M/Z=4
0.020
0.015
0.010
0.005
0
I_{RF}/I_{END}
Fit: y = c0[1−exp(−x/c1)]
c0 = 1.6e−02±8.6e−04
c1 = 3.4e+00±3.8e−01
0
2
4
6
8
10
12
14
Applied RF Power (W)

FIGURE 15

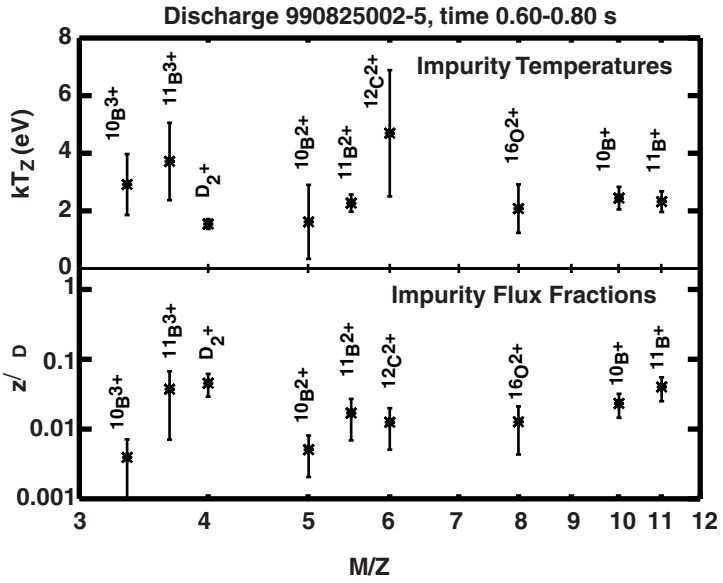
Discharge 990825002-5, time 0.60-0.80 s
Impurity Temperatures
Impurity Flux Fractions
kT_Z (eV)
z/ D
M/Z
10B3+
11B3+
D2+
10B2+
11B2+
12C2+
16O2+
10B+
11B+

FIGURE 16

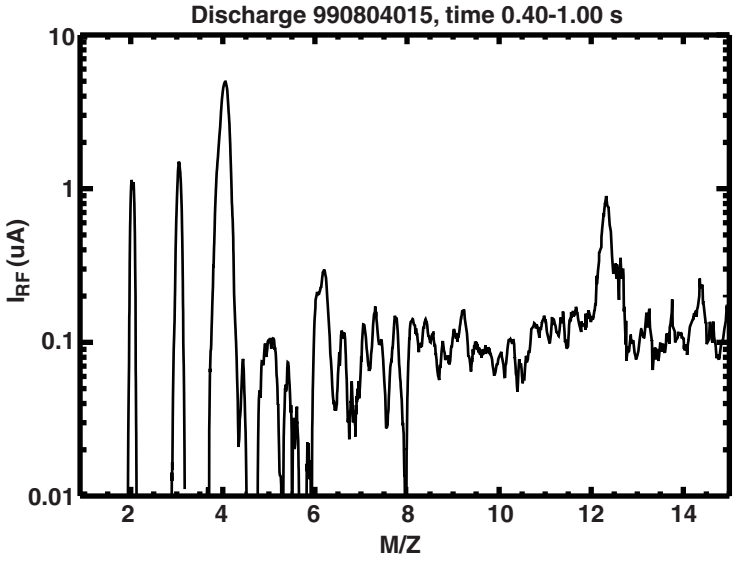
Discharge 990804015, time 0.40-1.00 s
10
1
0.1
0.01
I_{RF} (uA)
2
4
6
8
10
12
14
M/Z

FIGURE 17